Predicting streaming potential in reactive media: the role of pore geometry during dissolution and precipitation

M Soldi, L Guarracino, D Jougnot

Geophysical Journal International

Geophys. J. Int. (2024) **236,** 967–978
Advance Access publication 2023 November 28
GJI Rock and Mineral Physics, Rheology

https://doi.org/10.1093/gji/ggad457

Predicting streaming potential in reactive media: the role of pore geometry during dissolution and precipitation

M. Soldi,[1] L. Guarracino[1] and D. Jougnot[2]

[1]*Facultad de Ciencias Astronómicas y Geofísicas, Universidad Nacional de La Plata, CONICET, La Plata, Argentina. E-mail: msoldi@fcaglp.unlp.edu.ar*
[2]*Sorbonne Université, CNRS, EPHE, UMR 7619 Metis, F-75005, Paris, France*

Accepted 2023 November 15. Received 2023 November 14; in original form 2022 September 14

SUMMARY

Dissolution and precipitation processes modify the structure of the porous media at microscale which significantly affects the macroscopic properties of the media. These variations in the pore geometry result in changes in the hydraulic properties that control the groundwater flow, and also modify the electrokinetic properties associated to the displacement of electrical charges carried by the flow which originates the streaming potential. Under the hypothesis of a uniform dissolution or precipitation of the pores and based on the effective excess charge density approach, we present a physically based theoretical model for estimating the effective excess charge density as a function of time. The model is based on the assumption that the pore structure can be represented by an ensemble of capillary tubes with a smooth periodic variation of their radius and a fractal pore size distribution. The analytical expressions obtained to describe the effective excess charge density depend on the chemical parameters of the fluid and the petrophysical properties of the medium. In addition, the periodic variations assumed in the pore geometry represent a more realistic description of a porous medium than considering the pores as constant radii capillaries. These irregularities allow us to include the hysteresis phenomenon in the electrokinetic properties. The expressions of the proposed model have been tested with experimental data consisting of sets of effective excess charge density-effective saturation, permeability-effective saturation, porosity-time and permeability-time values. In all cases, the model is able to satisfactorily reproduce the behaviour of the data.

Key words: Electrical properties; Microstructure; Permeability and porosity; Fractals and multifractals; Hydrogeophysics.

1 INTRODUCTION

Flow and transport processes through porous media are strongly controlled by the structure of their pore system. When a reactive fluid circulates through a porous medium, the microscale structure of the pores is significantly affected by mineral dissolution and precipitation processes causing surface and volume variations that produce changes in the measurable properties at macroscale (e.g. Tartakovsky *et al.* 2007). These phenomena have a major impact when describing processes such as geothermal systems, CO_2 storage, flow and transport in unsaturated soils, electrokinetic coupling or oil recovery (e.g. Huber *et al.* 2010; Parmigiani *et al.* 2011; Cherubini *et al.* 2019). Hence, the characterization of the pore geometry and the flow properties at microscale is essential to describe and model the petrophysical properties at macroscale adequately.

Hydraulic and transport properties variations during dissolution and precipitation processes of the porous media have been widely studied in the literature. Among the works focused on chemical processes in the last decades, Bernabé *et al.* (2003) analysed the relationship between porosity and permeability during the time evolution of the media. They focused on how laboratory chemically driven processes (e.g. plastic compaction of aggregates, elastic-brittle deformation and microcracking) affect the evolution of the permeability–porosity relationship. Kang *et al.* (2003) used the lattice-Boltzmann method to simulate fluid flow, dissolution and precipitation in a porous medium reactive solid phase. They observed a wormhole phenomenon in which the initial main flow path becomes more dominant and a highly increase in permeability due to dissolution. Tartakovsky *et al.* (2007) studied numerically the reactive transport and mineral precipitation in porous and fractured porous media. This numerical model was used to estimate the mass transfer coefficient and reaction rate constants. Bolster *et al.* (2009) studied the impact of the geometry and molecular diffusion on effective solute dispersion of porous media and observed that dispersive effects increase monotonically with the amplitude of the pore radii for a fixed flow rate. Guarracino *et al.* (2014) derived an analytical model to predict the time evolution of continuum macroscale

properties of a porous medium in response to dissolution. Their model is able to estimate the hydraulic properties and the diffusive coefficient. Recently, Pereira Nunes *et al.* (2016) presented a particle-based method to simulate calcite dissolution on 3-D micro-CT images. This method is able to predict the evolution of hydraulic properties in carbonate rocks subjected to CO_2 brine injections.

Dissolution and precipitation processes also affect electrical and electrokinetic properties which can be used to characterize flow in porous media through petrophysical relationships (Binley & Kemna 2005). The electrical conductivity is related to electrical conduction in the electrolyte through the transport of charges by ions, while the electrokinetic properties are linked to the coupling between an electrical potential and fluid pressure gradients which rises when the electrolyte flows through the porous media. This electrical gradient is originated to maintain the electroneutrality when an excess of electrical charge at the solid-fluid interface is dragged by the water flow. Following the Gouy–Chapman–Stern model, the charged space in the electrolyte is divided into two layers: a compact layer (i.e. Stern) where most of the excess charge is distributed and fixed in the solid-fluid interface, and a diffuse layer (i.e. Gouy–Chapman) where the remaining excess charge is carried by the water flow. These layers are separated by a surface approximated by a plane called the plane of shear which is characterized by an electrical potential named zeta potential (Hunter 1981). In recent works, electrical conductivity and zeta potential models are used to describe chemical processes between the solid matrix and pore water. Guichet *et al.* (2006) studied the effect of mineral precipitation on the electrokinetic properties in terms of the pH profile of the zeta potential. The authors observed significant variations in the electrokinetic behaviour caused by changes in the sign of the zeta potential and a major reduction of its absolute values. Leroy *et al.* (2017) developed a model to estimate conductivity during calcite precipitation on glass beads. This model depends on the electrical charges at the Stern layer and the electrical potential at the onset of the diffuse layer. More recently, Niu & Zhang (2019) performed numerical simulations of dissolution and precipitation on digital representations of microstructural images to study the electrical conductivity through formation factor variations. They observed that the electrical conductivity is significantly influenced by the patterns of the mineral precipitation and dissolution. In transport-limited cases, the minerals are mostly near the pore throats which affects the electrical conductivity more than in reaction-limited cases where the minerals uniformly distribute at the solid–fluid interface.

The aim of this study is to describe the effect of pore geometry variations on the electrokinetic properties using the excess charge density approach. This approach assumes that the streaming current of the coupling phenomenon is generated by the water flow inside the pores that drags the fraction of the excess charge distributed in the diffuse layer (Sill 1983; Kormiltsev *et al.* 1998). The effective excess charge density $\hat{Q}_v$ (C m^{-3}) is a key parameter since it is directly related to the water flux velocity $\mathbf{v}$ (m s^{-1}):

$$\nabla \cdot (\sigma \nabla \varphi) = \nabla \cdot (\hat{Q}_v \mathbf{v}) \tag{1}$$

where φ (V) is the electrical potential and σ (S m^{-1}) the electrical conductivity. It is important to remark that to describe the effective excess charge density, the characterization of the water flow at microscale (i.e. pore scale) plays a key role to estimate this electrokinetic property at macroscale (e.g. laboratory scale). The pore space structure in which water flow occurs can be extremely irregular and complex for a real porous medium. In carbonate reservoir rocks the different geometries of the pores and the pore throats are the main controlling parameters of the water movements and entrapment (e.g. Aliakbardoust & Rahimpour-Bonab 2013). Therefore, the description at microscale of the pore structure and the flow properties is an important feature to estimate and study the hydraulic properties and thus the electrokinetic phenomenon at the macroscale. Nevertheless, the electrokinetic properties can also be studied by describing the streaming potential coupling coefficient C_{ek} (V Pa^{-1}) which relates electrical potential and fluid pressure differences (Helmholtz 1879; Smoluchowski 1903). This coefficient can be related to the effective excess charge from the previous approach as:

$$C_{ek} = -\frac{\hat{Q}_v k}{\mu \sigma} \tag{2}$$

where k (m^2) and μ (Pa s) are the permeability of the porous medium and the water dynamic viscosity, respectively.

Capillary tube models have been useful to characterize porous media since their simplicity to describe pore properties from the assumption of different pore shapes and pore size distributions. Whereas these models are a simple representation of the real pore space, they have been used to provide valuable insight into different topics of flow and transport in porous media (e.g. Yu *et al.* 2003; Jackson 2008; Jougnot *et al.* 2012; Wang *et al.* 2019; Rembert *et al.* 2020). Among the different pore size distributions considered for the bundle of capillaries (e.g. multimodal, quasi-fractal, fractal and Gaussian), fractal distributions have proven to be efficient to represent porous media due to their simplicity and capacity to describe a wide range of natural geological media (e.g. Tyler & Wheatcraft 1990; Yu 2008; Guarracino & Quintana 2009; Ghanbarian-Alavijeh *et al.* 2011). The use of fractal distributions presents the advantage of providing closed-form analytical equations for describing macroscale properties which allows a straightforward implementation of the models. Based on capillary tube models and fractal distributions, Jackson (2008), Guarracino & Jougnot (2018), Thanh *et al.* (2018), Soldi *et al.* (2019) and Thanh *et al.* (2020) have successfully developed analytical models to estimate the effective excess charge density under either total or partial saturation conditions of the porous medium. All these authors considered capillaries of constant radius in their analysis which is a good first approximation to study the electrokinetic phenomenon, however, it does not represent the intricate structure of a natural porous medium. Considering the irregularities present in the pores structure, Soldi *et al.* (2020) developed a physically based analytical model to describe the effective excess charge density including the hysteresis phenomenon. The authors introduced the irregularities in the pore geometry by considering each capillary as a cylindrical tube with periodic reductions of the capillary radius (i.e. consecutive segments of different constant radii). Rembert *et al.* (2020) derived an analytical fractal model to describe electrical conductivity in porous media assuming a capillary bundle of sinusoidal tortuous tubes. More recently and based on fractal geometry, Guarracino & Jougnot (2022) developed an analytical model to estimate the effective excess charge density for fractured porous media under partial and total saturation conditions.

In the framework of the excess charge density approach and capillary tube models, we derive a new analytical and physically based model to describe the effective excess charge density temporal evolution during dissolution and precipitation in a porous medium. For this purpose, we consider the pores represented by tubes of varying aperture which follow a sinusoidal piecewise function (Fig. 1). This geometry presents periodic reductions in the pore radius ('ink-bottle') which connect smoothly with the pore bodies (wide space

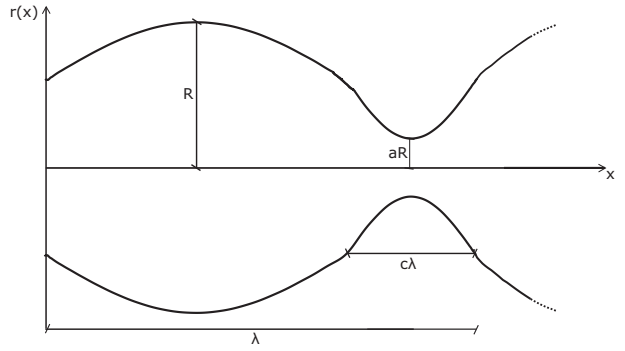

Figure 1. Pore geometry scheme for one wavelength of the proposed model.

of the pore) allowing to represent porous media with different hydraulic properties. The importance of this representation is that the pore throats strongly control the flow properties. In addition, this geometry presents an advantage over the geometry proposed by Soldi *et al.* (2020) since smooth variations of the pores radii are a more realistic representation of a natural porous medium than straight periodic reductions. Variations in the size of the pores during dissolution and precipitation produce changes in the flow and therefore in the description of the effective excess charge which is effectively dragged by the flow. Previous studies analysed the effect of dissolution and precipitation from chemical approaches (e.g. Bernabé *et al.* 2003), we focus our study on the role of geometry changes on the effective excess charge density and thus we neglect changes in the chemical parameters. Assuming the described sinusoidal geometry and a non-reactive flow, Soldi *et al.* (2022) derived the mathematical expressions for the hydraulic properties of the porous medium. The authors calculated the properties of a single capillary tube and then upscaled to a representative elementary volume (REV) by assuming a fractal distribution of capillaries. In order to obtain the electrokinetic properties of the medium, we follow the same upscaling derivation method proposed by Soldi *et al.* (2022). On the one hand, we estimate the effective excess charge density in a single capillary tube from the radial distributions of excess charge and water flow. On the other hand, the effective excess charge density for the REV is estimated using a flux-averaging technique. The pore space variations during dissolution are considered in the model by assuming that the porous medium is dissolved by a fluid that reacts uniformly with the surface of the pores. We describe the variation of the pore radii caused by dissolution to derive closed-form analytical expressions for the temporal evolution of the hydraulic and electrokinetic properties. The resulting expressions of the model to describe the effective excess charge density also depend on geometrical and chemical parameters of the model. In addition, the periodic constrictivities of the pores allow to include the hysteresis phenomenon of porous media in a simple form due to the strong control of those irregularities over the water flow. The proposed model expressions are compared against different sets of experimental laboratory data.

The article is organized in four main parts as follows. In Section 2, we describe the geometrical representation of the porous medium and derive the model equations. The resulting expressions describe the hydraulic properties (porosity, effective saturation, and saturated and relative permeability) and electrokinetic properties (saturated and relative effective excess charge density) during reactive processes. Then, in Section 3, we test the sensitivity of the effective excess charge density estimates during dissolution to changes in the model parameter values (i.e. the size of the pore throat aperture and the dissolution rate). In Section 4, we compare the model against different experimental data sets. We test the ability of the model to simultaneously estimate hydraulic and electrokinetic data for a non-reactive flow. We also examine the performance of the model to reproduce the behaviour of experimental data during dissolution. Finally, in Section 5, we discuss and summarize the results presented in this study.

2 MODEL DEVELOPMENT

The effective excess charge density is derived within the framework of bundles of capillary tubes for which we follow the pore geometrical description assumed by Soldi *et al.* (2022). In order to derive the model, we present the geometry and size-distribution of the pores from Soldi *et al.* (2022). Then, by considering the effect of dissolution in the pore geometry, we modify the expressions for the hydraulic properties from Soldi *et al.* (2022) to include the dissolution of the porous medium. Finally, we derive the electrokinetic properties for a single capillary and upscale this property to a REV of porous medium obtaining the effective excess charge density expressions during dissolution.

To represent the porous medium we consider a cylindrical REV of radius R_{REV} (m) and length L (m) whose pore structure is characterized by an ensemble of tortuous capillaries. Each capillary is conceptualized as a circular tube of radius R (m), hydraulic tortuosity τ (dimensionless) and length l (m) with periodic reductions of its radius (as shown in Fig. 1). Assuming that the pore geometry has a wavelength λ (m), the variable radius of each pore $r(x)$ (m) along one wavelength of the capillary can be expressed as:

$$r(x) = \begin{cases} \frac{R}{2}(1+a) + \frac{R}{2}(1-a)\sin\left(\frac{\pi}{\lambda(1-c)}x\right) & \text{if} \quad x \in [0, \lambda(1-c)), \\ \frac{R}{2}(1+a) + \frac{R}{2}(1-a)\sin\left(\frac{\pi}{\lambda c}[x-\lambda(1-2c)]\right) & \text{if} \quad x \in [\lambda(1-c), \lambda) \end{cases} \tag{3}$$

where a is the radial factor that represents the ratio in which the radius is reduced ($0 \leq a \leq 1$, dimensionless) and c the length factor ($0 \leq c \leq 1$, dimensionless) that represents the fraction of λ with narrowing radius. We assume that this geometry is replicated along each pore length an integer number M of wavelengths. Note that if $a = 1$ we obtain a capillary of constant radius R and if $a = 0$ the capillary tube is closed. In the case of $c = 0.5$, the narrow (i.e. pore throat) and wide (i.e. pore body) fractions of the sinusoidal pore geometry have the same length and eq. (3) is equivalent to the model of Guarracino *et al.* (2014).

The radii of the pores within the REV vary between a maximum $R_{\max}$ and a minimum $R_{\min}$ pore radius value. The cumulative pore size distribution is assumed to obey a fractal scaling law as follows (Tyler & Wheatcraft 1990; Yu 2008; Thanh *et al.* 2018; Guarracino & Jougnot 2018; Soldi *et al.* 2019, 2022):

$$N(R) = \left(\frac{R_{\mathrm{REV}}}{R}\right)^{D}, \tag{4}$$

where D is the pore fractal dimension (dimensionless) which varies between 1 and 2. Then, differentiating eq. (4) with respect to R, the number of pores with radius between R and $R + \mathrm{d}R$ is expressed as:

$$\mathrm{d}N(R) = -D R_{\mathrm{REV}}^{D} R^{-D-1} \mathrm{d}R. \tag{5}$$

The negative sign in eq. (5) implies that the pore number decreases with the increase of the pore radius and $-\mathrm{d}N > 0$ (Yu 2008).

The flow of a reactive fluid through the bundle of capillaries produces variations in the structure of each capillary tube. As a result, dissolution processes cause changes in the volume and surface at

pore scale. To estimate the geometrical changes, we assume that the pores are dissolved uniformly so that the circular shape of the cross-section of the tubes is not affected (i.e. it increases while keeping its natural shape). Then, the volume change with time t of each pore is assumed to be proportional to the surface of the tube S_p in contact with the reactive fluid and to the dissolution rate α which yields (Freedman *et al.* 2004; Guarracino *et al.* 2014):

$$\frac{\mathrm{d}V_p(R)}{\mathrm{d}t} = \alpha(R)S_p(R). \tag{6}$$

The dissolution rate α is expressed as a function of the pore radius due to large pores enlarging faster than the small ones during dissolution processes (e.g. Bekri *et al.* 1995). Hence, we assume a linear relationship between α and R, $\alpha(R) = \tilde{\alpha}R$, so that the dissolution is not very aggressive. Under this hypothesis, the fractal dimension and the radial and length factors can be assumed constant during the process. Integrating eq. (6), we obtain the radius of the pore as a function of time (Guarracino *et al.* 2014):

$$R(t) = R(t_0)e^{\beta(t-t_0)} \tag{7}$$

where t_0 (hr) is the initial time of the dissolution process and the factor β (hr^{-1}) is a function of the model parameters a, c and $\tilde{\alpha}$ (hr^{-1}) which yields:

$$\beta = \frac{\tilde{\alpha}[4\pi(1+a)c + (1-a)(1-2c)]}{2\pi(1+a)^2 + \pi(1-a)^2 + 8(1-a^2)(1-2c)}. \tag{8}$$

Note that as precipitation processes cause a reduction of the pore volume with time, under the same hypotheses and considering that parameter $\tilde{\alpha} < 0$, a similar expression to eq. (7) can be obtained, where $\beta < 0$, resulting in a decreasing radius with time. Fig. 2 shows the pore geometry evolution during dissolution and precipitation. We consider the following values of the model parameters as reference at the start of each process: $a = 0.4$, $c = 0.6$, $R = 0.1$ mm and $\tilde{\alpha} = 1 \times 10^{-4}$ hr^{-1}. It can be observed that the pore structure is less constrictive at the end of the dissolution process as a result of the increasing pore radius along its length during this process, otherwise, a precipitation process reduces the aperture of the pore which results in a more closed pore.

2.1 Hydraulic properties

The macroscopic hydraulic properties of the porous medium at a fixed time during the dissolution process can be described in terms of the geometrical parameters and the fractal size-distribution of the pores. Soldi *et al.* (2022) obtained expressions for the porosity ϕ and permeability k^{sat} given by:

$$\phi = \frac{f_v(a,c)D\tau}{R_{\mathrm{REV}}^{(2-D)}(2-D)}\left[R_{\max}^{2-D} - R_{\min}^{2-D}\right], \tag{9}$$

where the factor $f_v(a,c)$ is

$$f_v(a,c) = \frac{(1+a)^2}{4} + \frac{(1-a)^2}{8} + \frac{1}{\pi}(1-a^2)(1-2c) \tag{10}$$

and

$$k^{\mathrm{sat}} = f_k(a,c)\frac{DR_{\mathrm{REV}}^{D-2}}{8\tau(4-D)}\left[R_{\max}^{4-D} - R_{\min}^{4-D}\right] \tag{11}$$

where the factor $f_k(a,c)$ can be approximated by:

$$f_k(a,c) = \frac{a^{3/2}\pi(1+a)^3}{2\pi(1+a)^2 - 4(1-a)(1-2c)(1+\sqrt{a})^2}. \tag{12}$$

The factors f_v and f_k quantify the reduction in the porosity and permeability, respectively, due to the presence of constrictivities in the pores. These factors vary in the range from 0 to 1 and are dimensionless.

The evolution of porosity and permeability during dissolution processes can be obtained by considering the changes of the pore radii $R_{\min}$ and $R_{\max}$ with time. Substituting eq. (7) in eqs (9) and (11), the temporal variation of these macroscopic properties can be expressed as:

$$\phi(t) = \phi(t_0)e^{\beta(2-D)(t-t_0)} \tag{13}$$

$$k^{\mathrm{sat}}(t) = k^{\mathrm{sat}}(t_0)e^{\beta(4-D)(t-t_0)} \tag{14}$$

where $\phi(t_0)$ and $k^{\mathrm{sat}}(t_0)$ are the porosity and permeability of the REV at the initial time t_0 of the dissolution process, respectively.

The periodic reductions present in the pores radius cause different patterns of saturation during drainage and imbibition processes. Therefore, the sinusoidal geometry allows to describe the hysteresis phenomenon in the effective saturation S_e and relative permeability k_{rel} curves as functions of pressure head h (m). The pressure needed to drain or flood the REV is related to the pore throat radius R/a for the drainage process and to the radius of the pore body R for the imbibition through $h = 2T_s\cos(\gamma)/\rho g R^*$ where T_s (N m^{-1}) is the surface tension, γ (°) the contact angle, ρ (kg m^{-3}) the water density, g (m s^{-2}) the gravitational acceleration and $R^* = R/a$ or $R^* = R$ (e.g. Bear 1998; Soldi *et al.* 2017). The recent model from Soldi *et al.* (2022) estimates the hydraulic properties of a porous medium with the proposed geometry and for a drainage process the main drying effective saturation curve S_e^d can be expressed as a function of h as

$$S_e^d(h) = \frac{(ah)^{D-2} - h_{\max}^{D-2}}{h_{\min}^{D-2} - h_{\max}^{D-2}}. \tag{15}$$

Considering the link between h and R described above, and eqs (15) and (7), at each time of a dissolution process, the main drying effective saturation curve S_e^d as a function of pressure head for a drainage process yields

$$S_e^d(h,t) = \frac{(ah)^{D-2}e^{\beta(D-2)(t-t_0)} - h_{\max}^{D-2}(t_0)}{h_{\min}^{D-2}(t_0) - h_{\max}^{D-2}(t_0)} \tag{16}$$

where h varies between $h_{\min}(t_0)e^{-\beta(t-t_0)}/a$ and $h_{\max}(t_0)e^{-\beta(t-t_0)}/a$. Similarly, for an imbibition process, the main wetting effective saturation curve S_e^w can be expressed as

$$S_e^w(h,t) = \frac{h^{D-2}e^{\beta(D-2)(t-t_0)} - h_{\max}^{D-2}(t_0)}{h_{\min}^{D-2}(t_0) - h_{\max}^{D-2}(t_0)} \tag{17}$$

with h varying in the range from $h_{\min}(t_0)e^{-\beta(t-t_0)}$ to $h_{\max}(t_0)e^{-\beta(t-t_0)}$. The terms $h_{\min}(t_0)$ and $h_{\max}(t_0)$ are the minimum and maximum pressure heads at the beginning of the dissolution process t_0 given by

$$h_{\min}(t_0) = \frac{2T_s\cos(\gamma)}{\rho g R_{\max}(t_0)} \quad \text{and} \quad h_{\max}(t_0) = \frac{2T_s\cos(\gamma)}{\rho g R_{\min}(t_0)}, \tag{18}$$

where $R_{\min}(t_0)$ is the minimum radius and $R_{\max}(t_0)$ the maximum radius at the start of the process. By inspection of eq. (16) at a fixed time of the dissolution, note that if $h \le h_{\min}(t_0)e^{-\beta(t-t_0)}/a$, $S_e^d = 1$, the REV is fully saturated since the pressure head applied is lower than the one necessary to start draining the larger pores, and in the case of $h \ge h_{\max}(t_0)e^{-\beta(t-t_0)}/a$, $S_e^d = 0$ as the pressure head applied is large enough to drain the REV. Similar results can be obtained by analyzing eq. (17) for the wetting process, $S_e^w = 1$ and $S_e^w = 0$ when $h \le h_{\min}(t_0)e^{-\beta(t-t_0)}$ and $h \ge h_{\max}(t_0)e^{-\beta(t-t_0)}$, respectively.

Similarly, under the same hypotheses to drain and flood the REV and considering the Buckingham–Darcy law for unsaturated water

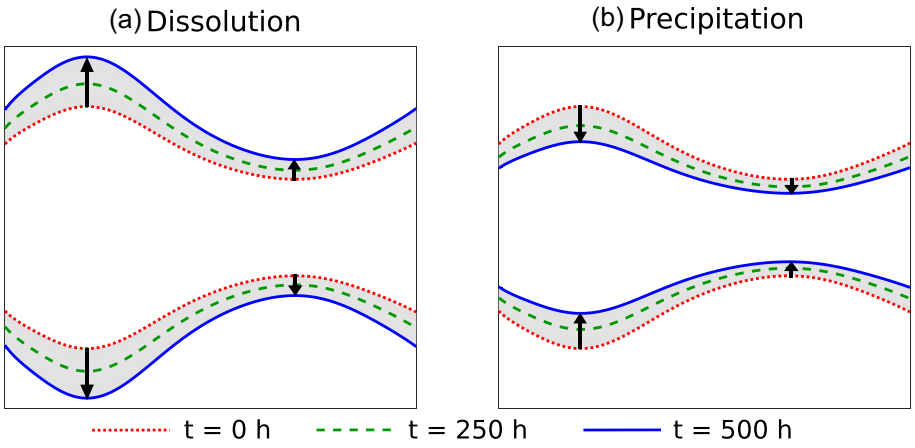

Figure 2. Schematic representation of the pore geometry evolution with time for: (a) a dissolution process and (b) a precipitation process.

flow, the main drying relative permeability curve k^d_{rel} for a drainage process during dissolution can be expressed as (following the work of Soldi *et al.* 2022):

$$k^d_{\text{rel}}(h,t) = \frac{(ah)^{D-4}e^{\beta(D-4)(t-t_0)} - h^{D-4}_{\text{max}}(t_0)}{h^{D-4}_{\text{min}}(t_0) - h^{D-4}_{\text{max}}(t_0)} \tag{19}$$

where h varies between $h_{\text{min}}(t_0)e^{-\beta(t-t_0)}/a$ and $h_{\text{max}}(t_0)e^{-\beta(t-t_0)}/a$, and the main wetting relative permeability curve k^w_{rel} for an imbibition process can be computed as:

$$k^w_{\text{rel}}(h,t) = \frac{h^{D-4}e^{\beta(D-4)(t-t_0)} - h^{D-4}_{\text{max}}(t_0)}{h^{D-4}_{\text{min}}(t_0) - h^{D-4}_{\text{max}}(t_0)} \tag{20}$$

where h varies between $h_{\text{min}}(t_0)e^{-\beta(t-t_0)}$ and $h_{\text{max}}(t_0)e^{-\beta(t-t_0)}$. Note that, by examining eq. (19) and the range of pressure head values at a fixed time of the dissolution, $k^d_{\text{rel}} = 1$ when $h \leq h_{\text{min}}(t_0)e^{-\beta(t-t_0)}/a$ since the applied pressure head is not large enough to drain the REV and $k^d_{\text{rel}} = 0$ when $h \geq h_{\text{max}}(t_0)e^{-\beta(t-t_0)}/a$ as the REV is drained by this pressure head. In the case of an imbibition process, $k^w_{\text{rel}} = 1$ if $h \leq h_{\text{min}}(t_0)e^{-\beta(t-t_0)}$, and $k^w_{\text{rel}} = 0$ if $h \geq h_{\text{max}}(t_0)e^{-\beta(t-t_0)}$ which result from the inspection of eq. (20) similarly to the drainage.

A relationship between the macroscopic hydraulic properties of the porous medium can be obtained to estimate permeability as a function of effective saturation at each time of a dissolution process. Combining eqs (16) and (19) for the drainage process, and (17) and (20) for the imbibition, at a given stage of the dissolution (a fixed time), we obtain a mathematical expression of $k_{\text{rel}}(S_e)$ which is the same for both the drainage and imbibition, and if we consider eq. (11), it yields:

$$k(S_e) = k^{\text{sat}}\frac{\left[S_e\left(\delta^{D-2}-1\right)+1\right]^{\frac{4-D}{2-D}}-1}{\delta^{D-4}-1} \tag{21}$$

where δ is the quotient between the minimum h_{min} and maximum h_{max} pressure heads at the considered stage of the dissolution process. Note that a non-hysteretic function is obtained when k is expressed as a function of S_e which is in agreement with a number of experimental data (e.g. Topp & Miller 1966; Van Genuchten 1980; Mualem 1986).

2.2 Electrokinetic properties

The electrokinetic phenomenon is caused by the coupling between the fluid flow and charge distribution at pore scale. We first estimate the effective excess charge density for a single pore and for a fixed time of the dissolution in order to derive the effective excess charge density at the macroscale. We consider that each capillary tube is saturated by a binary symmetric 1:1 electrolyte (e.g. NaCl) and that the flow regime is laminar. Under the assumption of an electrical double layer (EDL), we are interested in the layer in which the fluid flows (i.e. Gouy–Chapman layer) while the Stern layer can be neglected. The thickness of the Gouy–Chapman layer is defined by the so-called Debye length l_D (m) which for the assumed type of electrolyte is given by:

$$l_D = \sqrt{\frac{\varepsilon k_B T}{2N_A C^0_{\text{w}} e_0^2}}, \tag{22}$$

being ε (F m^{-1}) the pore water dielectric permittivity, N_A (mol^{-1}) Avogadro's number, e_0 (C) the elementary charge and C^0_{w} (mol l^{-1}) the ionic concentration. In the framework of an EDL and assuming that its thickness is much smaller than the pore radius, Guarracino & Jougnot (2018) found an expression for the effective excess charge density carried by the water flow in the Gouy–Chapman layer for a single pore of constant radius R and it yields:

$$\hat{Q}^R_v = \frac{8N_A e_0 C^0_{\text{w}}}{(R/l_D)^2}\left[-\frac{2e_0\zeta}{k_B T} - \left(\frac{e_0\zeta}{3k_B T}\right)^3\right], \tag{23}$$

where ζ (V) is the zeta potential, k_B (J K^{-1}) the Boltzmann constant and T (K) the temperature. eq. (23) is valid when the pore radii are greater than $5l_{\text{D}}$ (see Guarracino & Jougnot 2018; Jougnot *et al.* 2019).

To compute the effective excess charge density carried by the water flux in a capillary tube with varying radius $\hat{Q}^p_v$ (C m^{-3}), we assume the conservation of the electrical charges in the pore volume and then $\hat{Q}^p_v$ can be expressed as:

$$\hat{Q}^p_v(R) = \frac{1}{V_p}\int_0^l \hat{Q}^{r(x)}_v \pi r^2(x)dx = \hat{Q}^R_v\frac{1}{f_v} \tag{24}$$

being $V_p = \pi R^2 l f_v$ the volume of a single pore and f_v the factor given by eq. (10). Note that $\hat{Q}^p_v$ depends on the pore geometry parameters, a and c, through the factor f_v. Considering constant values of the length factor c, we analyse the effect of the radial factor a on $1/f_v$ as shown in Fig. 3. It is interesting to observe that for decreasing values of a, $1/f_v$ increases which leads to a large effect on the $\hat{Q}^p_v$ values due to a significant reduction of the pore radius. Hence, the constrictive geometry of the tubes plays a key role in the estimate of the effective excess charge density for each pore.

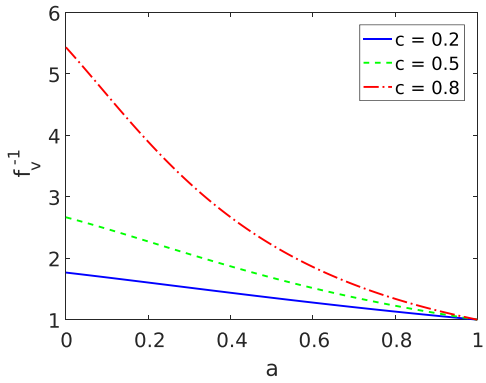

Figure 3. Dimensionless factor $1/f_v$ as a function of the radial factor a for different constant values of parameter c.

To derive the effective excess charge density $\hat{Q}_v^{\mathrm{REV}}$ at macroscale, we consider the previously defined REV of the porous medium under similar conditions of saturation to those used to compute the hydraulic properties. First, for a drainage process and at a given time during the dissolution, we assume that a pressure head h is applied to drain a fully saturated REV. In this case, only the pores that remain fully saturated contribute to the water flow ($R_{\min} \leq R \leq R_h/a$) and thus the drying effective excess charge density $\hat{Q}_v^{\mathrm{REV},d}$ (C m^{-3}) can be calculated as:

$$\hat{Q}_v^{\mathrm{REV},d} = \frac{1}{v_D \pi R_{\mathrm{REV}}^2} \int_{R_{\min}}^{\frac{R_h}{a}} \hat{Q}_v^p(R) q_p(R) \mathrm{d}N(R), \tag{25}$$

where $v_D = \frac{\rho g}{\eta} k_{\mathrm{rel}} k^{\mathrm{sat}} \frac{\Delta h}{L}$ (m s^{-1}) is Darcy's velocity and $q_p(R) = \frac{\rho g \pi}{\eta 8 \tau} R^4 f_k \frac{\Delta h}{L}$ (m^3 s^{-1}) the volumetric flow rate of a pore with varying aperture (see Soldi *et al.* 2022).

Substituting eqs (5) and (24) in (25) and combining the resulting expression with eqs (9) and (16), we obtain the expression of $\hat{Q}_v^{\mathrm{REV},d}$:

$$\hat{Q}_v^{\mathrm{REV},d} = N_A e_0 C_{\mathrm{w}}^0 \left[-\frac{2e_0\zeta}{k_B T} - \left(\frac{e_0\zeta}{3k_B T} \right)^3 \right] \frac{l_D^2}{\tau^2} \frac{f_k}{f_v^2} \frac{\phi}{k} \frac{S_e^d}{k_{\mathrm{rel}}^d}. \tag{26}$$

Similarly, in the case of an imbibition process, we consider that the REV is saturated with a pressure head h at a given time of the dissolution process. Therefore, the wetting effective excess charge density $\hat{Q}_v^{\mathrm{REV},w}$ can be computed by integrating eq. (25) over the range of fully saturated pores that contribute to the water flow ($R_{\min} \leq R \leq R_h$) and it yields:

$$\hat{Q}_v^{\mathrm{REV},w} = N_A e_0 C_{\mathrm{w}}^0 \left[-\frac{2e_0\zeta}{k_B T} - \left(\frac{e_0\zeta}{3k_B T} \right)^3 \right] \frac{l_D^2}{\tau^2} \frac{f_k}{f_v^2} \frac{\phi}{k} \frac{S_e^w}{k_{\mathrm{rel}}^w}. \tag{27}$$

Note that when $a = 1$ (i.e. non-constrictive tubes), $f_v = f_k = 1$ which leads to the same analytical expression for eqs (26) and (27). In this case, no hysteresis phenomenon will be present and the resulting expression is consistent with the one of the effective excess charge density for tortuous straight tubes obtained by Soldi *et al.* (2019).

The effective excess charge density for drainage and imbibition processes (eqs 26 and 27) can be expressed in general as:

$$\hat{Q}_v^{\mathrm{REV},i} = \hat{Q}_v^{\mathrm{REV,sat}} \hat{Q}_v^{\mathrm{REV,rel},i} \tag{28}$$

where

$$\hat{Q}_v^{\mathrm{REV,sat}} = N_A e_0 C_{\mathrm{w}}^0 \left[-\frac{2e_0\zeta}{k_B T} - \left(\frac{e_0\zeta}{3k_B T} \right)^3 \right] \frac{l_D^2}{\tau^2} \frac{f_k}{f_v^2} \frac{\phi}{k} \tag{29}$$

and

$$\hat{Q}_v^{\mathrm{REV,rel},i} = \frac{S_e^i}{k_{\mathrm{rel}}^i}, \tag{30}$$

being $\hat{Q}_v^{\mathrm{REV,sat}}$ (C m^{-3}) the effective excess charge density under saturated conditions and $\hat{Q}_v^{\mathrm{REV,rel},i}$ (dimensionless) the relative effective excess charge density where the superscript i refers to d or w, the drying or wetting case, respectively. It is interesting to note that while $\hat{Q}_v^{\mathrm{REV,sat}}$ depends on petrophysical and electrochemical properties, $\hat{Q}_v^{\mathrm{REV,rel},i}$ only depends on the hydraulic properties of the media, S_e and k_{rel}, which differ between drainage and imbibition processes. Hence, the saturated factor has the same expression for both processes, and the relative factor accounts for the hysteresis phenomenon present in the effective excess charge density.

The saturated effective excess charge density evolution with time during dissolution processes can be derived by considering the temporal variation of porosity and permeability. Substituting eqs (13) and (14) in eq. (29), we obtain the expression of $\hat{Q}_v^{\mathrm{REV,sat}}$ as function of time:

$$\hat{Q}_v^{\mathrm{REV,sat}}(t) = \hat{Q}_v^{\mathrm{REV,sat}}(t_0) e^{-2\beta(t-t_0)} \tag{31}$$

where $\hat{Q}_v^{\mathrm{REV,sat}}(t_0)$ is the saturated effective excess charge density of the REV at the start of the dissolution process. Note that eq. (31) has a closed-form analytical expression that depends on the geometrical parameters of the model a and c, and the dissolution rate $\tilde{\alpha}$ through the factor β (eq. 8).

The main curves of $\hat{Q}_v^{\mathrm{REV,rel}}$ for drainage and imbibition processes during dissolution can be obtained when this relative effective excess charge density is expressed as a function of pressure head h and time t. Substituting eqs (16) and (19) in (30), the main drying relative effective excess charge density $\hat{Q}_v^{\mathrm{REV,rel},d}$ is expressed as:

$$\hat{Q}_v^{\mathrm{REV,rel},d}(h,t) = \begin{cases} 1 \\ \text{if} \quad h \leq \frac{h_{\min}(t_0)}{a} e^{-\beta(t-t_0)} \\ \\ \frac{(ah)^{D-2} e^{\beta(D-2)(t-t_0)} - h_{\max}^{D-2}(t_0)}{(ah)^{D-4} e^{\beta(D-4)(t-t_0)} - h_{\max}^{D-4}(t_0)} \cdot \frac{h_{\min}^{D-4}(t_0) - h_{\max}^{D-4}(t_0)}{h_{\min}^{D-2}(t_0) - h_{\max}^{D-2}(t_0)} \\ \text{if} \quad \frac{h_{\min}(t_0)}{a} e^{-\beta(t-t_0)} < h < \frac{h_{\max}(t_0)}{a} e^{-\beta(t-t_0)} \\ \\ \frac{(D-2)}{(D-4)} \frac{h_{\min}^{D-4}(t_0) - h_{\max}^{D-4}(t_0)}{h_{\min}^{D-2}(t_0) - h_{\max}^{D-2}(t_0)} h_{\max}^2(t_0) \\ \text{if} \quad h \geq \frac{h_{\max}(t_0)}{a} e^{-\beta(t-t_0)}. \end{cases} \tag{32}$$

Similarly, from eqs (17) and (20), the main wetting relative effective excess charge density curve $\hat{Q}_v^{\mathrm{REV,rel},w}$ is given by:

$$\hat{Q}_v^{\mathrm{REV,rel},w}(h,t) = \begin{cases} 1 \\ \text{if} \quad h \leq h_{\min}(t_0) e^{-\beta(t-t_0)} \\ \\ \frac{h^{D-2} e^{\beta(D-2)(t-t_0)} - h_{\max}^{D-2}(t_0)}{h^{D-4} e^{\beta(D-4)(t-t_0)} - h_{\max}^{D-4}(t_0)} \cdot \frac{h_{\min}^{D-4}(t_0) - h_{\max}^{D-4}(t_0)}{h_{\min}^{D-2}(t_0) - h_{\max}^{D-2}(t_0)} \\ \text{if } h_{\min}(t_0) e^{-\beta(t-t_0)} < h < h_{\max}(t_0) e^{-\beta(t-t_0)} \\ \\ \frac{(D-2)}{(D-4)} \frac{h_{\min}^{D-4}(t_0) - h_{\max}^{D-4}(t_0)}{h_{\min}^{D-2}(t_0) - h_{\max}^{D-2}(t_0)} h_{\max}^2(t_0) \\ \text{if} \quad h \geq h_{\max}(t_0) e^{-\beta(t-t_0)}. \end{cases} \tag{33}$$

The limit value in eqs (32) and (33) for $h \geq h_{\max}(t_0) e^{-\beta(t-t_0)}/a$ and $h \geq h_{\max}(t_0) e^{-\beta(t-t_0)}$ is obtained by inspection of eq. (30) when S_e approaches zero since both terms of the quotient approaches to zero for drainage (when $h \to h_{\max}(t_0) e^{-\beta(t-t_0)}/a$) and imbibition (when

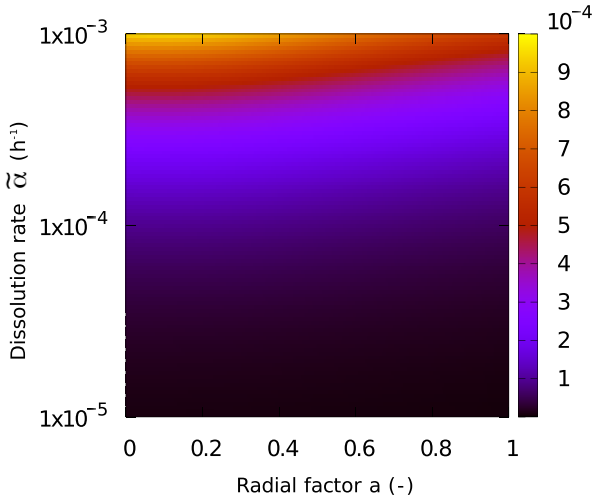

Figure 4. Parametric analysis of the dimensionless factor β as a function of the dissolution rate $\tilde{\alpha}$ and the radial factor a, for a constant value of the length factor $c = 0.6$.

$h \rightarrow h_{\max}(t_0)e^{-\beta(t-t_0)}$). This value represents the limit case in which a residual water saturation drags the excess charge in the pores with the smallest radii.

Note that eqs (26), (27), (29), (31), (32) and (33) which estimate the total, saturated and relative effective excess charge density at macroscale during a dissolution process have analytical and closed-form expressions which depend on petrophysical and electrokinetic properties of the porous medium and on independent parameters of the model with physical or geometrical meaning.

3 SENSITIVITY ANALYSIS OF THE MODEL

The role of the model parameters in the estimates of the effective excess charge density during dissolution is studied by a parametric analysis of parameter β (eq. 8) and of the relative effective excess charge density given by eqs (32) and (33). We test the influence of the radial factor a which controls the aperture of the pore throats and the dissolution rate $\tilde{\alpha}$ as these parameters produce the strongest impact on the geometry of the porous media.

Fig. 4 summarizes the analysis of parameter β (eq. 8) for the following ranges of variability of the radial factor a and the dissolution rate $\tilde{\alpha}$: $0 \leq a \leq 1$ and $1 \times 10^{-5}\text{hr}^{-1} \leq \tilde{\alpha} \leq 1 \times 10^{-3}$ hr^{-1}. Parameter β also requires specifying the length factor c for which we assume $c = 0.6$ as reference value. Note that for a fixed value of the radial factor a, the values of parameter β increase with increasing values of the dissolution rate $\tilde{\alpha}$ as faster dissolutions will produce more significant changes for a given pore geometry. It can also be observed that for low values of the dissolution rate, parameter β presents no significant changes for all the range of the radial factor values which could be associated with the slight variations in the radii due to very low dissolution processes.

The influence of the radial factor a on the main drying and wetting curves of $\hat{Q}_v^{\text{REV,rel}}$ (eqs 32 and 33) at the beginning and at the end of dissolution is illustrated in Figs 5(a)–(c). These equations also require specifying parameters D, $\tilde{\alpha}$, $R_{\min}$ and $R_{\max}$ for which we consider the following reference values: $D = 1.5$, $\tilde{\alpha} = 5 \times 10^{-4}$ hr^{-1}, $R_{\min}(t_0) = 1.5 \times 10^{-4}$ mm and $R_{\max}(t_0) = 1.5 \times 10^{-1}$ mm, being $t_0 = 0$ hr. The radial factor a strongly affects the hysteresis cycle as it is directly related to the pressure head limit values of the main $\hat{Q}_v^{\text{REV,rel}}$ curve for the drainage. For low values of a, the hysteresis cycle of $\hat{Q}_v^{\text{REV,rel}}$ increases as the difference in the pressure head limit values increase between the drainage and imbibition. During dissolution, the increase of the radii of the pores causes a decrease in the pressure head values needed to drain or flood the medium (see eq. 18). As a result of a medium with larger pores, the hysteresis cycle that corresponds to the final stage of dissolution is displaced to the left of the hysteresis cycle from the beginning of the process. Figs 5(d)–(f) show the influence of the dissolution rate $\tilde{\alpha}$ on the estimates of $\hat{Q}_v^{\text{REV,rel}}$ for a reference value of $a = 0.5$ and the previously reference values taken for D, $R_{\min}(t_0)$ and $R_{\max}(t_0)$. Variations of this parameter also produce a shift in the main drying curves of the effective excess charge density. For increasing values of $\tilde{\alpha}$, the hysteresis cycles at the initial and final stages present the strongest difference since increasing displacements to the left can be observed due to the larger pores obtained from higher dissolution rates.

From this parametric analysis, we can conclude that the dissolution rate $\tilde{\alpha}$ strongly affects parameter β and that fast dissolution processes cause the most significant changes in this parameter. Note that β is associated to the saturated effective excess charge density $\hat{Q}_v^{\text{REV,sat}}$ (eq. 31). Therefore, strong variations of this parameter will produce significant variations in the magnitude of $\hat{Q}_v^{\text{REV,sat}}$. Furthermore, both the radial factor a and the dissolution rate $\tilde{\alpha}$ affect the relative effective excess charge density $\hat{Q}_v^{\text{REV,rel}}$. The hysteresis cycles of $\hat{Q}_v^{\text{REV,rel}}$ increase for more constrictive pores (low values of a) and the distance between the initial and final cycles during dissolution increases for high dissolution rates $\tilde{\alpha}$ due to the strong difference between the initial and final sizes of the pore radii.

4 COMPARISON WITH EXPERIMENTAL DATA

4.1 Electrokinetic and hydraulic data for non-reactive flow

In order to test the proposed model, we perform a joint inversion of hydraulic and electrokinetic laboratory data sets measured during a non-reactive flow experiment. We selected data series from Cherubini *et al.* (2018) which consist of permeability k and effective excess charge density $\hat{Q}_v^{\text{REV}}$ values for three carbonate rock samples, named BRAU2, ESTA2 and RFF2. The fit between the $\hat{Q}_v^{\text{REV}}$ and k estimates of the model (eqs 28 and 21) and the experimental data sets is performed by using an exhaustive search method which is a simple and robust technique to find the best model parameters when only a few of them are unknown. This method selects the parameters that minimize the weighted normalized error between calculated and experimental data values for both $\hat{Q}_v^{\text{REV}}$ and k curves simultaneously. To reduce the number of the fitting parameters to D, a, c, $h_{\min}$ and $h_{\max}$, the REV radius R_{REV} and the ionic concentration C_w^0 values are taken from Cherubini *et al.* (2018), the zeta potential is estimated as function of C_w^0 using eq. (26) from Cherubini *et al.* (2018) and we consider $\tau = 1.1$ as a representative value of the tortuosity.

Fig. 6 shows the fitting curves of the proposed model to the data sets and the fitted parameters (D, a, c, $h_{\min}$ and $h_{\max}$) are listed in Table 1. The proposed model produces a fairly good agreement with the $\hat{Q}_v^{\text{REV}}$ data sets for all the samples, while also reproducing the behaviour of the k data. The geometry of the pores given by the fitted parameters presents strong radius variations as illustrated in Figs 6(c), (f) and (i). The low values of the radial factor a mean that the radii of the pores are significantly reduced in the

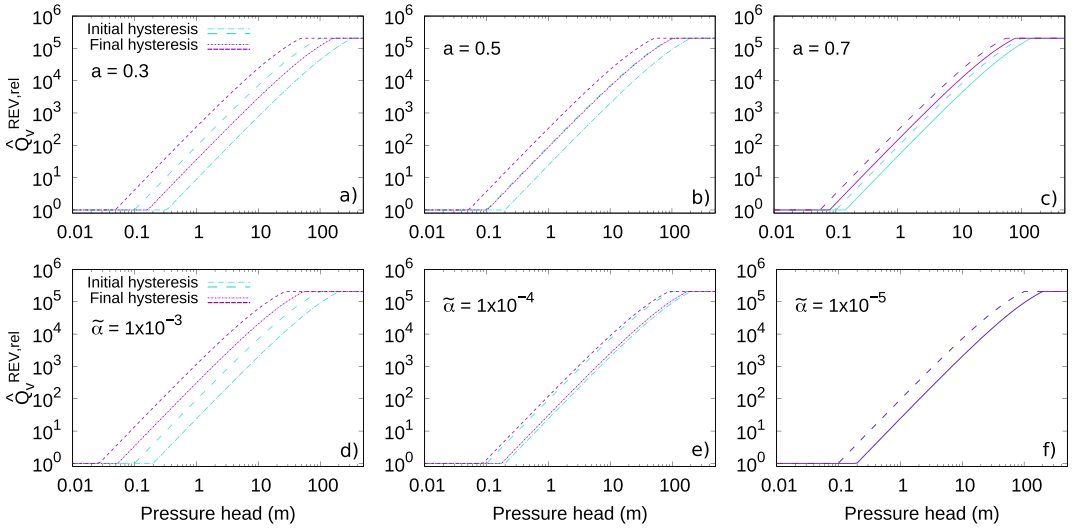

Figure 5. Curves of the main drying and wetting relative effective excess charge density at the initial and final stages of the dissolution: (a)–(c) sensitivity to the radial factor a, and (d)–(f) sensitivity to the dissolution rate $\tilde{\alpha}$. Note that the point-dashed and dashed lines correspond to the drainage and imbibition cases, respectively.

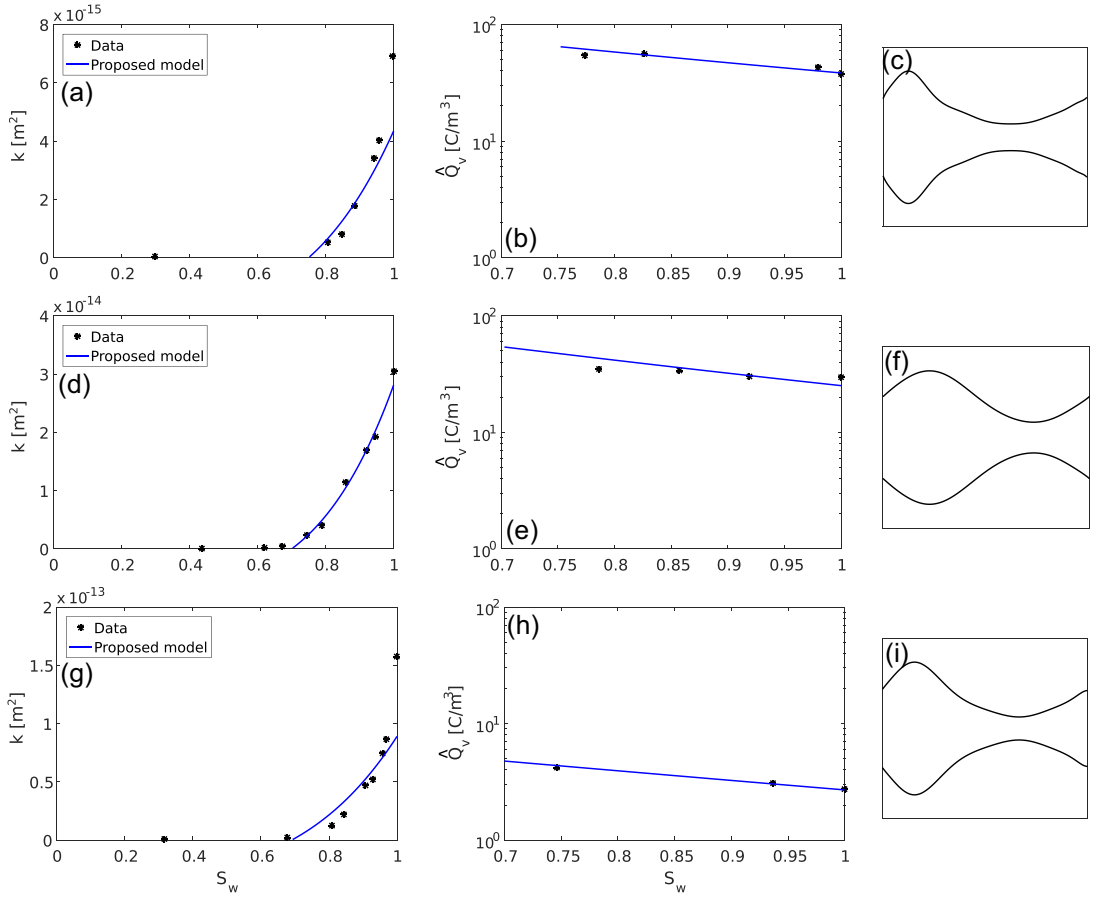

Figure 6. Comparison of the permeability and the effective excess charge density estimated by the proposed model with experimental data: (a–b) BRAU2, (d–e) ESTA2 and (g–h) RFF2 (data from Cherubini *et al.* 2018). Panels (c), (f) and (i) show schematic representations of the pore structure for the fitted parameters a and c.

pore throat which can be expected as carbonate rocks may present a large volume in the non-constrictive section of the pore while highly decreasing it in the constrictive section (Aliakbardoust & Rahimpour-Bonab 2013). Moreover, most of the k values are found in a narrow range of high S_w values since a sharp decreasing rate of the permeability and a high residual water saturation. This behaviour is consistent with the pore geometry represented by the fitted values of a as small pore throats mean high pressure head and

Table 1. Values of the fitted parameters to estimate the effective excess charge density and permeability for the data sets from Cherubini *et al.* (2018).

Sample	D	a	c	$h_{\min}$ (m)	$h_{\max}$ (m)
BRAU2	1.26	0.19	0.87	0.85	1.35
RFF2	1.38	0.18	0.68	0.79	1.41
ESTA2	1.58	0.23	0.55	0.92	1.64

therefore a high residual water saturation (Wang *et al.* 1991). Note that with only one set of the model parameters we can estimate both the hydraulic and electrokinetic properties simultaneously.

4.2 Estimation of $\hat{Q}_v^{\mathrm{REV}}$ during dissolution

The performance of the model to describe the dissolution phenomenon on the hydraulic and electrokinetic properties is tested by using available hydraulic data from the literature. To test the model, it would be desirable to get simultaneously experimental data of the evolution of porosity ϕ, permeability k and saturated effective excess charge density $\hat{Q}_v^{\mathrm{REV,sat}}$ during the process. However, data sets of $\hat{Q}_v^{\mathrm{REV,sat}}$ during dissolution experiments are lacking thus far in the literature. Jové Colón *et al.* (2004) studied the effect of dissolution on a clay-free sandstone laboratory sample. They measured the temporal evolution of porosity and permeability with the sample at a temperature of 80 °C. Hence, we fit our model (eqs 13 and 14) to the experimental data of ϕ and k, and estimate the evolution of $\hat{Q}_v^{\mathrm{REV,sat}}$ with time (eq. 31). To determine the value of $\hat{Q}_v^{\mathrm{REV,sat}}$ at the start of the dissolution we considered the ionic concentration C_{w}^0 and the REV radius R_{REV} values from Jové Colón *et al.* (2004) while the zeta potential is calculated using the relationship proposed by Jaafar *et al.* (2009) which estimates ζ as function of C_{w}^0. Moreover, by considering the initial and final stages of the dissolution, we analyse the variations in the relative effective excess charge density $\hat{Q}_v^{\mathrm{REV,rel}}$ which includes the hysteresis phenomenon.

The proposed model is fitted using an exhaustive search method by minimizing the weighted normalized error between the calculated and measured values of ϕ and k simultaneously. Figs 7(a) and (b) show the fit of eqs (13) and (14), respectively, and Fig. 7(c) illustrates the evolution of predicted $\hat{Q}_v^{\mathrm{REV,sat}}$ by the proposed model (eq. 31). The values of the fitted parameters are: $a = 0.24$, $c = 0.46$, $D = 1.46$, $\tau = 1.80$, $R_{\min} = 1.0 \times 10^{-6}$ cm, $R_{\max} = 1.9 \times 10^{-3}$ cm and $\tilde{\alpha} = 3.68 \times 10^{-4}$ hr^{-1}. Note that the dissolution rate $\tilde{\alpha}$ can be expressed in units of mol length^{-2} time^{-1} by using the relationship proposed by Menke *et al.* (2015) which depends on both the specific surface area and the number of moles per unit volume. Estimating the surface area through porosity (Bear 1998) and taking the number of moles from Jové Colón *et al.* (2004), it yields a dissolution rate of 1.5×10^{-9} mol cm^{-2} s^{-1} whose value lies within the range $10^{-8} - 10^{-12}$ mol cm^{-2} s^{-1} reported from experimental and numerical studies of reactive processes (e.g. Chou *et al.* 1989; Ruiz-Agudo *et al.* 2009; Vinogradov *et al.* 2022). Note that the evolution over time of both ϕ and k of the experimental data can be satisfactorily reproduced by the proposed model, as shown in Fig. 7. It is important to remark that we focus our analysis on the effect of pore geometry changes due to dissolution on the macroscopic properties. Therefore, variations of other parameters during the process, for example ionic concentration, are neglected (for chemical changes see Rembert *et al.* (2022)). The proposed model predicts a decreasing magnitude of $\hat{Q}_v^{\mathrm{REV,sat}}$, which can be related to the fact that permeability can increase more significantly than porosity due to dissolution of the pore throat radii (less constrictive pores). Fig. 7(d) shows the predicted values of $\hat{Q}_v^{\mathrm{REV,rel}}$ for the drainage (eq. 32) and imbibition (eq. 33) at the initial and final stages of the dissolution. Note that the hysteresis cycle at the end of the dissolution can be distinguished from the hysteresis cycle at the beginning. This result is directly linked to the dissolution rate $\tilde{\alpha}$ value and can be associated with a fast dissolution which produces a significant increase in the size of the pores radii and therefore a decrease in the corresponding pressure head values. Moreover, for drainage and imbibition, $\hat{Q}_v^{\mathrm{REV,rel}}$ shows a monotonic behaviour as a function of the pressure head (Fig. 7d). Indeed, $\hat{Q}_v^{\mathrm{REV,rel}}$ is controlled by the hydraulic properties of the porous media, its magnitude increases as the pressure head increases which is related to a decreasing water saturation and is consistent with the behaviour shown in previous studies (e.g. Jougnot *et al.* 2012; Zhang *et al.* 2017; Soldi *et al.* 2019). It is worth mentioning that the hysteresis phenomenon included in the proposed model originates from irregularities in the pore structure, that is 'ink-bottle' effect. However, Zhang *et al.* (2017) observed differences in $\hat{Q}_v^{\mathrm{REV,rel}}$ when expressed as a function of water saturation between drainage and imbibition processes and attributed this phenomenon to contact angle effects. Nevertheless, other effects could also explain or contribute to the hysteresis phenomenon, such as network effects and film flow.

5 DISCUSSION AND CONCLUSION

The present study is focused on the role of pore geometry on the electrokinetic properties during dissolution and precipitation processes. We derived a physically based theoretical model to estimate the effective excess charge density temporal evolution under the assumption of a uniform dissolution of the pore space. The porous medium is represented by an ensemble of tortuous capillary tubes with a sinusoidal variation of tube radius along its length. Considering a fractal description of the pore size distribution, analytical closed-form expressions have been obtained for the effective excess charge density $\hat{Q}_v^{\mathrm{REV}}$ as a function of time. These expressions also depend on the chemical parameters of the pore water and on the petrophysical properties and geometrical parameters of the medium. It is worth mentioning that this model focuses only on the geometrical changes that dissolution produces on the pore structure while chemical parameters are considered constant during the process. Note also that the streaming potential variations during dissolution can be simulated using the proposed model through eq. (1) or the coupling coefficient by eq. (2).

The periodic variations in the radius of the pores allowed us to include the hysteresis phenomenon in the $\hat{Q}_v^{\mathrm{REV}}$. Both the relative and saturated effective excess charge density factors are affected by the pore geometry, whereas $\hat{Q}_v^{\mathrm{REV,rel}}$ is strongly influenced by the radial factor a which controls the size of the pore throats, $\hat{Q}_v^{\mathrm{REV,sat}}$ is affected by a and the length factor c through the f_k and f_v factors. In the limit case of tubes with constant radii ($a = 1$), the expressions of those factors are consistent with the expressions obtained by Soldi *et al.* (2019) for tortuous tubes of constant radius.

Pore geometry variations due to dissolution affect parameter β which is directly linked to the saturated effective excess charge density factor $\hat{Q}_v^{\mathrm{REV,sat}}$. Therefore, strong variations of this parameter produce important changes on the $\hat{Q}_v^{\mathrm{REV,sat}}$ values. The effect of reactive processes is also observed in the relative factor $\hat{Q}_v^{\mathrm{REV,rel}}$ resulting in shifts of the main drying and wetting curves of the hysteresis cycles caused by changes in the pressure head values due to variations on the pore radius sizes. It is important to remark

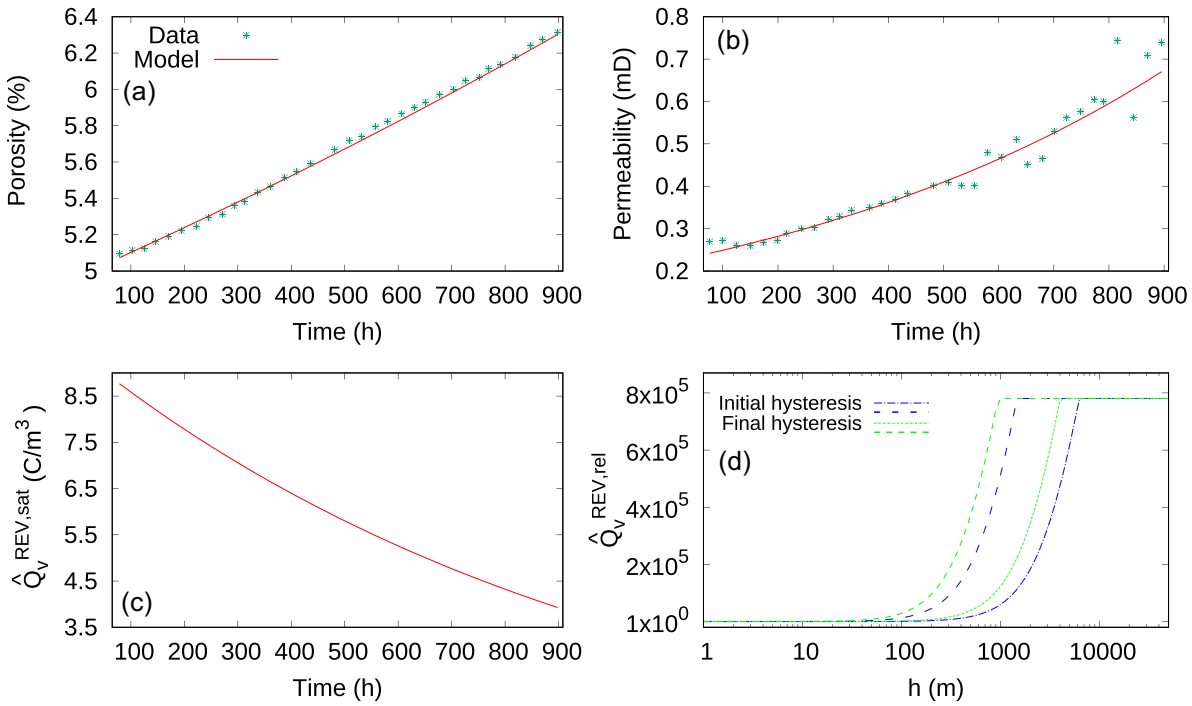

Figure 7. Model fit to the time evolution of: (a) porosity and (b) permeability data from Jové Colón *et al.* (2004), (c) estimates of the saturated effective excess charge density and (d) predicted relative effective excess charge density for the initial and final stages of the dissolution process. The point-dashed and dashed lines correspond to the main $\hat{Q}_v^{REV,rel}$ curves for drainage and imbibition processes, respectively.

that during dissolution parameter β is considered a positive value, however, the proposed model can be used to describe precipitation processes in a simple way by changing the sign of that parameter.

The proposed model expressions to estimate the effective excess charge density $\hat{Q}_v^{REV}$ and permeability k as functions of saturation are tested against sets of experimental data. The proposed model is able to fairly reproduce the $\hat{Q}_v^{REV}$ values and the behaviour of the k data from the fitting of only one set of the model parameters for both properties simultaneously.

To the best of our knowledge, there are no experimental effective excess charge density $\hat{Q}_v^{REV}$ data during a dissolution. However, a first test of the model was performed by comparing the temporal evolution predicted by the proposed model for the hydraulic properties against experimental data sets. The model is able to simultaneously fit the porosity and permeability data and predicts a decrease in the $\hat{Q}_v^{REV,sat}$ values. This first comparison is a starting point to show the ability of the proposed model to represent the effect of dissolution on the properties of a porous medium. The analysis of the relative effective excess charge density $\hat{Q}_v^{REV,rel}$ predicted for the initial and final stages of the dissolution shows that the main difference is a shift of the hysteresis cycle to lower pressure head values. This results from the increase of the pore radius which produces a decrease in the pressure head values needed to flood or drain the medium.

Based on the approach of the effective excess charge density, the proposed model represents a step forward to describe the electrokinetic properties during dissolution and precipitation of a porous medium. Pore geometry changes produced by these processes result in variations of the effective excess charge density under both total and partially saturated conditions. Moreover, the proposed geometry is a more realistic representation of a natural porous medium than previous capillary tube models and allows to include the hysteresis phenomenon in the electrokinetic coupling in a simple way. This analytical model can be a valuable starting point to look into the evolution of electrokinetic properties over time which may play an important role in processes related to petroleum reservoirs, geological sequestration of CO_2, diagenesis, bio-remediation of soils and environmental contaminant transport.

ACKNOWLEDGMENTS

The authors strongly thank the Editor Jana Börner, Assistant Editor Fern Storey, and the reviews of Jan Vinogradov and an anonymous reviewer for their careful assessment of our work and their constructive comments and suggestions.

DATA AVAILABILITY

No original data, everything has been published before.

REFERENCES

Aliakbardoust, E. & Rahimpour-Bonab, H., 2013. Effects of pore geometry and rock properties on water saturation of a carbonate reservoir, *J. Petrol. Sci. Eng.,* **112,** 296–309.

Bear, J., 1998. *Dynamics of Fluids in Porous Media,* Dover Publications, Inc.. ISBN: 9780486656755.

Bekri, S., Thovert, J. & Adler, P., 1995. Dissolution of porous media: Chem. eng, *Chem. Eng. Sci.,* **50**(17), 2765–2791.

Bernabé, Y., Mok, U. & Evans, B., 2003. Permeability-porosity relationships in rocks subjected to various evolution processes, *Pure appl. Geophys.,* **160**(5), 937–960.

Binley, A. & Kemna, A., 2005. Dc resistivity and induced polarization methods, in *Hydrogeophysics,* pp. 129–156, Springer.

Bolster, D., Dentz, M. & Le Borgne, T., 2009. Solute dispersion in channels with periodically varying apertures, *Phys. Fluids,* **21**(5), doi:10.1063/1.3131982.

Cherubini, A., Garcia, B., Cerepi, A. & Revil, A., 2018. Streaming potential coupling coefficient and transport properties of unsaturated carbonate rocks, *Vadose Zone J.,* **17**(1), 1–12.

Cherubini, A., Garcia, B., Cerepi, A. & Revil, A., 2019. Influence of CO_2 on the electrical conductivity and streaming potential of carbonate rocks, *J. geophys. Res.,* **124**(10), 10 056–10 073.

Chou, L., Garrels, R.M. & Wollast, R., 1989. Comparative study of the kinetics and mechanisms of dissolution of carbonate minerals, *Chem. Geol.,* **78**(3–4), 269–282.

Freedman, V.L., Bacon, D.H., Saripalli, K.P. & Meyer, P.D., 2004. A film depositional model of permeability for mineral reactions in unsaturated media, *Vadose Zone J.,* **3**(4), 1414–1424.

Ghanbarian-Alavijeh, B., Millán, H. & Huang, G., 2011. A review of fractal, prefractal and pore-solid-fractal models for parameterizing the soil water retention curve, *Can. J. Soil Sci.,* **91**(1), 1–14.

Guarracino, L. & Jougnot, D., 2018. A physically based analytical model to describe effective excess charge for streaming potential generation in water saturated porous media, *J. geophys. Res.,* **123**(1), 52–65.

Guarracino, L. & Jougnot, D., 2022. A fractal model for effective excess charge density in variably saturated fractured rocks, *J. geophys. Res.,* **127**(3), e2021JB022982.

Guarracino, L. & Quintana, F., 2009. A constitutive model for water flow in unsaturated fractured rocks, *Hydrol. Process.,* **23**(5), 697–701.

Guarracino, L., Rötting, T. & Carrera, J., 2014. A fractal model to describe the evolution of multiphase flow properties during mineral dissolution, *Adv. Water Resour.,* **67,** 78–86. doi:10.1016/j.advwatres.2014.02.011.

Guichet, X., Jouniaux, L. & Catel, N., 2006. Modification of streaming potential by precipitation of calcite in a sand–water system: laboratory measurements in the ph range from 4 to 12, *J. geophys. Int.,* **166**(1), 445–460.

Helmholtz, H.V., 1879. Studien über electrische grenzschichten, *Ann. Phys.,* **243**(7), 337–382.

Huber, C., Bachmann, O. & Manga, M., 2010. Two competing effects of volatiles on heat transfer in crystal-rich magmas: thermal insulation vs defrosting, *J. Petrol.,* **51**(4), 847–867.

Hunter, R., 1981. *Zeta Potential in Colloid Science: Principles and Applications,* Elsevier B.V.

Jaafar, M., Vinogradov, J. & Jackson, M., 2009. Measurement of streaming potential coupling coefficient in sandstones saturated with high salinity nacl brine, *Geophys. Res. Lett.,* **36**(21), doi:10.1029/2009GL040549.

Jackson, M.D., 2008. Characterization of multiphase electrokinetic coupling using a bundle of capillary tubes model, *J. geophys. Res.,* **113**(4), doi:10.1029/2007JB005490.

Jougnot, D., Linde, N., Revil, A. & Doussan, C., 2012. Derivation of soil-specific streaming potential electrical parameters from hydrodynamic characteristics of partially saturated soils, *Vadose Zone J.,* **11**(1), doi:10.2136/vzj2011.0086.

Jougnot, D., Mendieta, A., Leroy, P. & Maineult, A., 2019. Exploring the effect of the pore size distribution on the streaming potential generation in saturated porous media, insight from pore network simulations, *J. geophys. Res.,* **124,** 5315–5335. doi:10.1029/2018JB017240.

Jové Colón, C.F., Oelkers, E.H. & Schott, J., 2004. Experimental investigation of the effect of dissolution on sandstone permeability, porosity, and reactive surface area, *Geochim. Cosmochim. Acta,* **68**(4), 805–817.

Kang, Q., Zhang, D. & Chen, S., 2003. Simulation of dissolution and precipitation in porous media, *J. geophys. Res.,* **108**(B10), doi:10.1029/2003JB002504.

Kormiltsev, V.V., Ratushnyak, A.N. & Shapiro, V.A., 1998. Three-dimensional modeling of electric and magnetic fields induced by the fluid flow movement in porous media, *Phys. Earth planet. Inter.,* **105**(3–4), 109–118.

Leroy, P., Li, S., Jougnot, D., Revil, A. & Wu, Y., 2017. Modelling the evolution of complex conductivity during calcite precipitation on glass beads, *J. geophys. Int.,* **209**(1), 123–140.

Menke, H.P., Bijeljic, B., Andrew, M.G. & Blunt, M.J., 2015. Dynamic three-dimensional pore-scale imaging of reaction in a carbonate at reservoir conditions, *Environ. Sci. Technol.,* **49**(7), 4407–4414.

Mualem, Y., 1986. Hydraulic conductivity of unsaturated soils: prediction and formulas, in *Methods of Soil Analysis: Part 1 Physical and Mineralogical Methods,* 2nd edn, pp. 799–823, ed. Klute, A., Wiley.

Niu, Q. & Zhang, C., 2019. Permeability prediction in rocks experiencing mineral precipitation and dissolution: a numerical study, *Water Resour. Res.,* **55**(4), 3107–3121.

Parmigiani, A., Huber, C., Bachmann, O. & Chopard, B., 2011. Pore-scale mass and reactant transport in multiphase porous media flows, *J. Fluid Mech.,* **686,** 40–76. doi:10.1017/jfm.2011.268.

Pereira Nunes, J., Blunt, M. & Bijeljic, B., 2016. Pore-scale simulation of carbonate dissolution in micro-CT images, *J. geophys. Res.,* **121**(2), 558–576.

Rembert, F., Jougnot, D. & Guarracino, L., 2020. A fractal model for the electrical conductivity of water-saturated porous media during mineral precipitation-dissolution processes, *Adv. Water Resour.,* **145,** doi:10.1016/j.advwatres.2020.103742.

Rembert, F., Jougnot, D., Luquot, L. & Guérin, R., 2022. Interpreting self-potential signal during reactive transport: application to calcite dissolution and precipitation, *Water,* **14**(10), doi:10.3390/w14101632.

Ruiz-Agudo, E., Putnis, C., Jiménez-López, C. & Rodriguez-Navarro, C., 2009. An atomic force microscopy study of calcite dissolution in saline solutions: the role of magnesium ions, *Geochim. Cosmochim. Acta,* **73**(11), 3201–3217.

Sill, W.R., 1983. Self-potential modeling from primary flows, *Geophysics,* **48**(1), 76–86.

Smoluchowski, M., 1903. Contribution à la théorie de l'endosmose électrique et de quelques phénomènes corrélatifs, *Bull. Akad. Sci. Cracovie.,* **8,** 182–200. doi:10.1051/jphystap:019040030091201.

Soldi, M., Guarracino, L. & Jougnot, D., 2017. A simple hysteretic constitutive model for unsaturated flow, *Transp. Porous Media,* **120**(2), 271–285.

Soldi, M., Jougnot, D. & Guarracino, L., 2019. An analytical effective excess charge density model to predict the streaming potential generated by unsaturated flow, *J. geophys. Int.,* **216**(1), 380–394.

Soldi, M., Guarracino, L. & Jougnot, D., 2020. An effective excess charge model to describe hysteresis effects on streaming potential, *J. Hydrol.,* **588,** doi:10.1016/j.jhydrol.2020.124949.

Soldi, M., Guarracino, L. & Jougnot, D., 2022. The effect of pore geometry in constitutive hysteretic models for unsaturated water flow, *Environ. Fluid Mech.,* **22,** 1283–1305. doi:10.1007/s10652-022-09891-0.

Tartakovsky, A.M., Meakin, P., Scheibe, T.D. & Wood, B.D., 2007. A smoothed particle hydrodynamics model for reactive transport and mineral precipitation in porous and fractured porous media, *Water Resour. Res.,* **43**(5), doi:10.1029/2005WR004770.

Thanh, L.D., Van Do, P., Van Nghia, N. & Ca, N.X., 2018. A fractal model for streaming potential coefficient in porous media, *Geophys. Prospect.,* **66**(4), 753–766.

Thanh, L.D., Jougnot, D., Do, P.V., Ca, N.X. & Hien, N.T., 2020. A physically based model for the streaming potential coupling coefficient in partially saturated porous media, *Water,* **12**(6), doi:10.3390/w12061588.

Topp, G.C. & Miller, E., 1966. Hysteretic moisture characteristics and hydraulic conductivities for glass-bead media1, *Soil Sci. Soc. Am. J.,* **30**(2), 156–162.

Tyler, S.W. & Wheatcraft, S.W., 1990. Fractal processes in soil water retention, *Water Resour. Res.,* **26**(5), 1047–1054.

Van Genuchten, M.T., 1980. A closed-form equation for predicting the hydraulic conductivity of unsaturated soils, *Soil Sci. Soc. Am. J,* **44**(5), 892–898.

Vinogradov, J. *et al.*, 2022. Predictive surface complexation model of the calcite-aqueous solution interface: the impact of high concentration and complex composition of brines, *J. Colloid Interf. Sci.,* **609,** 852–867. doi:10.1016/j.jcis.2021.11.084.

Wang, F., Jiao, L., Zhao, J. & Cai, J., 2019. A more generalized model for relative permeability prediction in unsaturated fractal porous media, *J. Nat. Gas Sci. Eng.,* **67,** 82–92. doi:10.1016/j.jngse.2019.04.019.

Wang, Z., Hirsche, W. & Sedgwick, G., 1991. Electrical and petrophysical properties of carbonate rocks, in *SPE Annual Technical Conference and Exhibition,* OnePetro.

Yu, B., 2008. Analysis of flow in fractal porous media, *Appl. Mech. Rev.,* **61**(5), doi:10.1115/1.2955849.

Yu, B., Li, J., Li, Z. & Zou, M., 2003. Permeabilities of unsaturated fractal porous media, *Int. J. Multiphase Flow,* **29**(10), 1625–1642.

Zhang, J., Vinogradov, J., Leinov, E. & Jackson, M., 2017. Streaming potential during drainage and imbibition, *J. geophys. Res.,* **122**(6), 4413–4435.